Journal of Hydroscience and Hydraulic Engineering
Vol. 27, No.2 November, 2009, 29-47

RANS COMPUTATIONS ON CURVED OPEN CHANNEL FLOWS

By

Ichiro Kimura

Graduate School of Engineering, Hokkaido University, N13, W8, Kita-ku, Sapporo, Japan

Takashi Hosoda

Graduate School of Engineering, Kyoto University, Kyoto Daigaku, Katsura, Nishikyo-ku, Kyoto, Japan

Shinji Takimoto

Graduate School of Engineering, Hokkaido University, N13, W8, Kita-ku, Sapporo, Japan

and

Yasuyuki Shimizu

Graduate School of Engineering, Hokkaido University, N13, W8, Kita-ku, Sapporo, Japan

SYNOPSIS

Turbulent flow structures in curved open channel flows are important topics in river engineering from the viewpoints of both flood control and river environment. The turbulence structures are mainly dominated by the formations of cross-sectional secondary currents. The main circulation in a cross section is classified into the secondary current of the first kind, which is caused by the local unbalance of centrifugal force and lateral pressure gradient. An additional vortex called an outer-bank cell is generated near the corner between the surface and the outer-bank. Though the scale of the outer-bank cell is much smaller than the main secondary current, the outer-bank cell might have a strong influence on the erosion of the outer-bank because it is generated very close to the bank. Previous studies have shown that the outer-bank cell is initiated by two combinational effects, for example, turbulence anisotropy and the local unbalance of the centrifugal force and pressure gradient. Therefore, the criterion of the outer-bank cell is rather complicated and has not been clarified yet.

In this study, applicability of numerical models with RANS type turbulence models for simulating the outer-bank cell is examined. Both linear and non-linear k-ε models are applied to the mildly curved open channel flows investigated experimentally by Booij (1). First, a grid sensitivity analysis was carried out to determine an appropriate grid resolution. The numerical results showed that only non-linear models could capture the outer-bank cell and could reproduce velocity and Reynolds stress profiles satisfactory. The third order non-linear model slightly improved the accuracy compared with the second order model. The computations with different curvature radii indicate that the linear k-ε models can also generate the outer-bank cell in cases where there is a very sharp bend.

The threshold of R/H by the standard model for generation of the outer-bank cell was 22. The model with a lower eddy viscosity could yield the outer-bank cell in case of larger R/H.

INTRODUCTION

The cross sectional flow structure at a curved channel is a classical topic in fluid mechanics. It is important to clarify the detailed 3D turbulent flow structures in rivers from the viewpoints of both river environment and flood control. In straight open channel flows, the secondary current (flow normal to main flow direction) is induced by anisotropy of turbulence. This kind of current is known as the secondary current of the second kind, which is much weaker than the main flow. In flows at open channel bends, the secondary current becomes conspicuous due to the effect of the unbalance of the centrifugal force and local pressure gradient. The secondary current at open channel bends, which is called the secondary current of the first kind, has a significant effect on bed transform in river bends because the magnitude of the secondary current of the first kind is larger than that of second kind. The secondary current of the first kind conveys the flow near the surface toward the outer-bank and flow near the bottom toward the inner bank. Such flows generally induce the bed scouring near the outer-bank and deposition near the inner-bank. Around a corner between a free surface and an outer-bank, a small scale circulation in the opposite direction, which is referred to as an outer-bank cell, is generated. Though the scale of the outer-bank cell is much smaller than the main circulation of the secondary current of the first kind, the outer-bank cell might play an important role on the erosion of a bank because it occurs very close to the outer-bank. It has been shown that the outer-bank cell is generated not only in a turbulent flow but also in a laminar flow. In a laminar flow, the outer-bank cell is the result of the unbalance of the centrifugal force and the local pressure gradient under inverse velocity profile in a vertical direction. In a turbulent flow, the mechanism of the generation of an outer-bank cell becomes more complicated. Blanckaert et al. (2) showed through their laboratory tests that both the unbalance between the centrifugal force and the local pressure gradient, and the turbulence anisotropy affect the generation of the outer-bank cell.

Numerical studies focusing on the outer-bank cell have been done by several researchers. Booij (1) carried out computations of a flow in a mild curved open channel with a curvature radius, R = 4.1 m and Reynolds number, Re = 10^4 using both LES approach with the Smagorinsky type SGS model and RANS approach with the standard linear k-ε model. Only LES could reproduce the outer-bank cell. Christensen et al. (3) computed the open channel flow in a very sharp bend ($R/H < 16$, R: curvature radius, H: mean depth) and showed that the standard linear k-ε model could generate the outer-bank cell. Jia et al. (4) showed that the outer-bank cell can be reproduced using a second order non-linear k-ε model. Those results indicate that the turbulence model without the effects of anisotropy is not applicable to reproduce the outer-bank cell in the case of a mildly curved channel. However, applicability of non-linear RANS models for simulating the outer-bank cell has not been clarified yet.

It is important from an engineering point of view to clarify governing parameters and their thresholds for generating the outer-bank cell. In a laminar flow, the Dean number (= $\mathrm{Re}(H/R)^{0.5}$) can be considered as the only governing parameter. However, in a turbulent flow, the phenomenon is more complicated. De Vriend (5) pointed out that an eddy viscosity affects significantly the generation of the outer-bank cell and suggested a modified Dean number, De', which is obtained by replacing a dynamic viscosity ν in the Dean number by a eddy viscosity ν_t (De' = $\mathrm{De}\cdot(\nu/\nu_t)$). In cases of turbulent flows, since multiple parameters are related to the phenomena, further investigations are necessary to determine the governing parameters. It is not easy to clarify the threshold of the generation of the outer-bank cell in laboratory tests because the outer-bank cell is a small-scale phenomenon compared with the secondary current of the first kind. Therefore, computations are only practical approaches. It is important to develop a computational model, which can replicate the detailed turbulence structures with reasonable accuracy as well as computational efficiency.

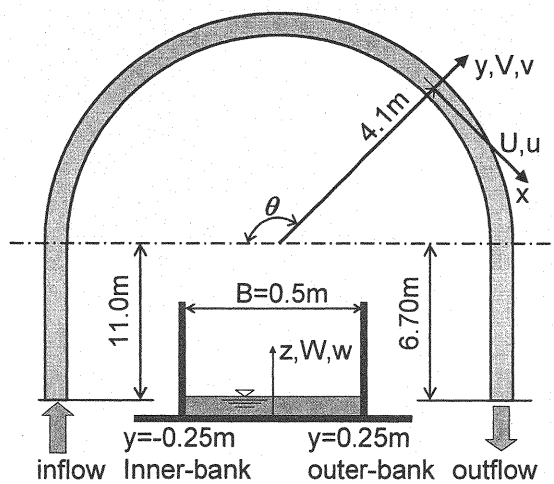

Fig.1 Plan and cross-sectional views of the experimental flume (Booij, 2003 (1))

Table 1 Hydraulic conditions in the laboratory test

H(cm)	U_a(cm/s)	R(m)	Re	Fr	De
5.0	20.0	4.1	10^4	0.29	1100

H: mean depth, U_a: mean velocity, Re: Reynolds number($=HU_a/\nu$),
Fr: Froude number ($=U_a/(gH)^{1/2}$, De: Dean number ($=\mathrm{Re}(H/R)^{1/2}$),
R: curvature radius at the channel bend

In this study, linear and non-linear k-ε models are applied to a mild curved open channel flow. The computations are performed under the same conditions as the laboratory test performed by Booij (1). First, a grid sensitivity analysis is performed and an appropriate grid resolution is found. Two types of computational domain, i.e., whole U-shape channel and small element of circular channel with cyclic boundary conditions, are examined. The latter computation corresponds to a well developed curved channel flow in an infinite circular channel. The effects of the non-linear order of the constitutive equation for the Reynolds stresses, and the curvature radius on the outer-bank cell are also elucidated by making a comparison with the experimental results. The computational results demonstrate clearly that the current RANS type model can efficiently reproduce the fundamental turbulence structures around a curved open channel.

OUTLINE OF THE LABORATORY TEST BY BOOIJ (2003)

Booij (1) performed a laboratory test on a mild curved open channel flow by using a U-type experimental flume schematically shown in Fig. 1. The channel consists of an 11m long straight inlet part, a semicircular curved part and a 6.7m long straight outlet part. The curvature radius of the semicircular part is R = 4.1m and the channel width is B = 50cm. The hydraulic conditions in the experiment are tabulated in Table 1.

Velocity distributions at a cross-section of θ= 135° were measured by using LDV. 6 min measurement was done at each point and time-mean velocities were obtained. Fig. 2 shows the measured time-mean flow pattern at the vicinity of the outer-bank. We can see two clear vortices. The larger vortex rotating in the clockwise direction is the secondary current of the first kind caused by the unbalance of the centrifugal force and the local pressure gradient. The smaller vortex on the right side near the surface rotating in the anti-clockwise direction is the outer-bank cell.

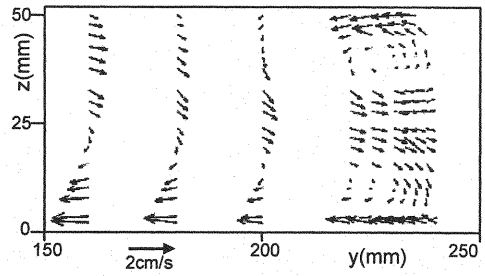

Fig. 2 Cross-sectional flow pattern in the laboratory test by Booij (2003) (θ=135°)

COMPUTATIONAL METHOD

Basic Equations

The Reynolds averaged 3D flow equations with contravariant components of velocity vectors on a generalized curvilinear movable coordinate system are used as governing equations. The equations are expressed as follows.

[Continuity equation]

$$\frac{1}{\sqrt{g}}\frac{\partial V^{\alpha}\sqrt{g}}{\partial \xi^{\alpha}} = 0 \tag{1}$$

[Momentum equations]

$$\frac{\partial V^i}{\partial t} + \nabla_j\left[V^i(V^j - W^j)\right] + V^i\nabla_j W^j + V^j\nabla_j W^i = F^i - \frac{1}{\rho}g^{ij}\nabla_j p + \nabla_j\left[-\overline{v^i v^j}\right] + 2\nu\nabla_j e^{ij} \tag{2}$$

[k equation]

$$\frac{\partial k}{\partial t} + \nabla_j\left[k(V^j - W^j)\right] + k\nabla_j W^j = -g_{il}\overline{v^i v^j}\nabla_j V^i - \varepsilon + \nabla_j\left\{\left(\frac{\nu_t}{\sigma_k} + \nu\right)g^{ij}\nabla_i k\right\} \tag{3}$$

[ε equation]

$$\frac{\partial \varepsilon}{\partial t} + \nabla_j\left[\varepsilon(V^j - W^j)\right] + \varepsilon\nabla_j W^j = -C_{\varepsilon 1}\frac{\varepsilon}{k}g_{il}\overline{v^i v^j}\nabla_j V^i - C_{\varepsilon 2}\frac{\varepsilon^2}{k} + \nabla_j\left\{\left(\frac{\nu_t}{\sigma_k} + \nu\right)g^{ij}\nabla_i \varepsilon\right\} \tag{4}$$

where ξ^i = generalized curvilinear coordinate, t = time, V^i = contravariant component of the velocity vector, W^i = contravariant component of the velocity vector of grid motion, p = pressure, ν = molecular kinematic viscosity, ρ = density of water, k = turbulent kinetic energy, ε = turbulent energy dissipation rate, ν_t = eddy viscosity coefficient, g_{ij} and g^{ij} = covariant and contravariant component of metric tensor, g = det(g_{ij}) and F^i = contravariant component of gravitational acceleration. ∇_i represents a covariant differential operator, for instance,

$$\nabla_i A^k = \frac{\partial A^k}{\partial \xi^i} + A^j\Gamma_{ij}{}^k \tag{5}$$

where Γ_{ij}^{k} = Christoffel's symbol described as

$$\Gamma_{ij}^{\ k} = \begin{Bmatrix} k \\ i\,j \end{Bmatrix} = \frac{1}{2} g^{km}\left(\frac{\partial g_{jm}}{\partial \xi^i} + \frac{\partial g_{im}}{\partial \xi^j} - \frac{\partial g_{ij}}{\partial \xi^m}\right) = \frac{\partial \xi^k}{\partial x^p}\frac{\partial^2 x^p}{\partial \xi^i \partial \xi^j} \tag{6}$$

The metric tensors are calculated by

$$g_{ij} = \frac{\partial x^k}{\partial \xi^i}\frac{\partial x^l}{\partial \xi^j}\delta_{kl},\ g^{ij} = \frac{\partial \xi^k}{\partial x^i}\frac{\partial \xi^l}{\partial x^j}\delta_{kl},\ g_{ij}g^{jk} = \delta_i^k \tag{7}$$

$C_{\varepsilon 1}$, $C_{\varepsilon 2}$, σ_k and σ_ε in Eqs. 3 and 4 are model constants ($C_{\varepsilon 1}$=1.44, $C_{\varepsilon 2}$=1.92, σ_k=1.0 and σ_ε=1.3 are used).

Turbulence Models

We adopted two-equation RANS type models while considering their computational efficiency. In order to consider the effect of turbulence anisotropy, three types of turbulence models with different orders, i.e., the linear standard k-ε model, the second order non-linear k-ε model and the third order non-linear k-ε model, were applied.

(1) Standard liner model

The constitutive equation of the standard linear k-ε model is:

$$-\overline{v^{'i}v^{'j}} = \nu_t S^{ij} - \frac{2}{3}k\delta_s^i g^{sj},\ \nu_t = C_\mu \frac{k^2}{\varepsilon} \tag{8}$$

where ν_t =eddy viscosity and C_μ = 0.09 (=const.).

(2) The second order non-linear k-ε model

The constitutive equation of the second order non-linear k-ε model in the generalized curvilinear coordinates is expressed as:

$$-\overline{v^{'i}v^{'j}} = \nu_t S^{ij} - \frac{2}{3}k\delta_s^i g^{sj} - \frac{k}{\varepsilon}\nu_t\left[\alpha_1 Q_1 + \alpha_2 Q_2 + \alpha_3 Q_3\right] \tag{9}$$

$$\nu_t = C_\mu \frac{k^2}{\varepsilon} \tag{10}$$

$$Q_1 = S^{i\alpha}g_{\alpha l}\Omega^{lj} + S^{j\beta}g_{\beta l}\Omega^{li} \tag{11}$$

$$Q_2 = S^{i\alpha}g_{\alpha l}S^{lj} - \frac{1}{3}S^{k\alpha}g_{\alpha m}S^{m\beta}g_{\beta k}\delta_l^i g^{lj} \tag{12}$$

$$Q_3 = \Omega^{i\alpha}g_{\alpha l}\Omega^{lj} - \frac{1}{3}\Omega^{k\alpha}g_{\alpha m}\Omega^{m\beta}g_{\beta k}\delta_l^i g^{lj} \tag{13}$$

$$S^{ij} = g^{j\alpha}\nabla_\alpha V^i + g^{i\alpha}\nabla_\alpha V^j,\ \Omega^{ij} = g^{j\alpha}\nabla_\alpha V^i - g^{i\alpha}\nabla_\alpha V^j \tag{14}$$

The model coefficients are essentially not constants but functions of the strain parameter S and the rotation parameter Ω (e.g., Kimura and Hosoda (6)). In this study, the following coefficients proposed by Ali et al. (7) are adopted.

$$\alpha_1 = -0.1325 f_M,\ \alpha_2 = 0.0675 f_M, \alpha_3 = -0.0675 f_M \tag{15}$$

$$f_M = \left(1 + m_{ds}S^2 + m_{d\Omega}\Omega^2\right)^{-1} \tag{16}$$

$$C_\mu = c_{\mu o}\left(1 + c_{ns}S^2 + c_{n\Omega}\Omega^2\right)/D_\mu \tag{17}$$

Table 2 Model constants of the second order non-linear k-ε model (Ali, Hosda & Kimura, 2007 (7))

$C_{\mu 0}$	0.09
m_{dS}	0.01
$m_{d\Omega}$	0.003
c_{nS}	0.0028
$c_{n\Omega}$	0.007
c_{dS}	0.0085
$c_{d\Omega}$	0.004
$c_{dS\Omega}$	0.003
c_{dS1}	0.00005
$c_{d\Omega 1}$	0.00005
$c_{dS\Omega 1}$	0.00025

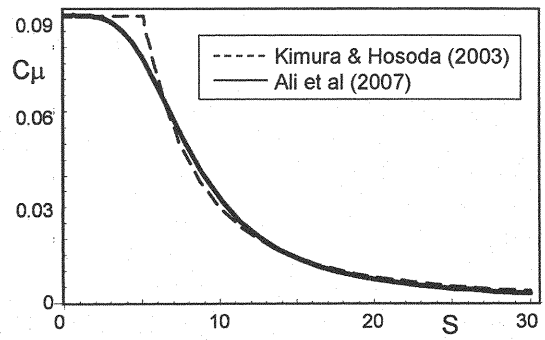

Fig.3 Comparison of function $C_\mu(S, \Omega)$ on $S = \Omega$ in two non-linear k-ε models

$$D_\mu = 1 + c_{dS} S^2 + c_{d\Omega} \Omega^2 + c_{dS\Omega} S\Omega + c_{dS1} S^4 + c_{d\Omega 1} \Omega^4 + c_{dS\Omega 1} S^2 \Omega^2 \tag{18}$$

$$S = \frac{k}{\varepsilon} \sqrt{\frac{1}{2} S^{i\alpha} g_{\alpha j} S^{j\beta} g_{\beta i}}, \quad \Omega = \frac{k}{\varepsilon} \sqrt{\frac{1}{2} \Omega^{i\alpha} g_{\alpha j} \Omega^{j\beta} g_{\beta i}} \tag{19}$$

The values of the model constants in Eqs. 16 - 18 are listed in Table 2. These constants were tuned considering realizability, distributions of turbulence intensities in a simple shear flow and distributions of Reynolds stresses around a Stuart vortex. The detailed process of tuning the model constants has been reported by Ali et al. (7). Kimura and Hosoda (6) proposed a simpler second order non-liner k-ε model, which includes the effects of the strain and the rotation parameters in the model coefficients. The model coefficients in Kimura and Hosoda (6) are expressed as

$$C_1 = \frac{0.4}{1 + 0.02\Phi^2}, \quad C_2 = 0, \quad C_3 = -\frac{0.13}{1 + 0.02\Phi^2}, \quad C_\mu = \min\left(0.09, \frac{0.3}{1 + 0.09\Phi^2}\right) \tag{20a,b,c,d}$$

where $\Phi = \max[S, \Omega]$. The model has been applied to the flow behind a square cylinder with Karman vortex shedding and flows around a cube. The approach utilizing $\Phi = \max[S, \Omega]$ is similar to the one used in the previous study by Craft et al. (8). Such models seem to be effective in reducing the number of model parameters and simplify the model. However the models contain a physical drawback. Fig. 3 shows the comparison of profiles of two different expressions by Kimura and Hosoda (6) and Ali et al. (7) for C_μ along the line of $S = \Omega$. The profiles of two functions are surprisingly very similar even though the two functions are derived in different ways. However, the 2D profiles on S–Ω plane in those two functions are considerably different as shown in Fig. 4. The function of Kimura

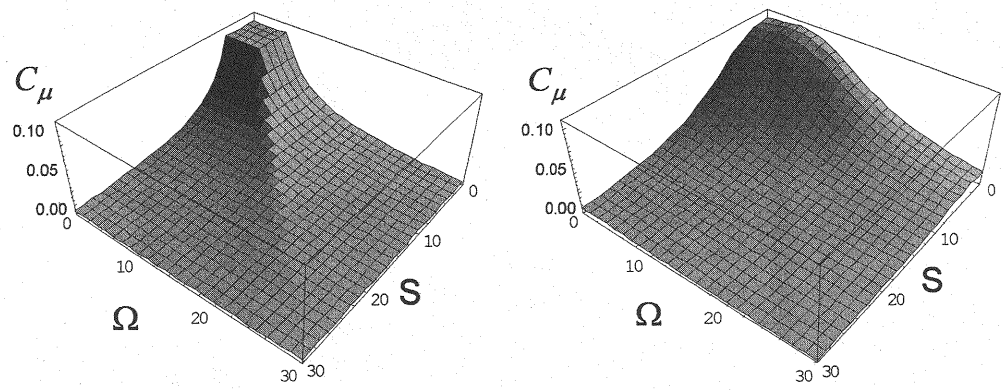

Fig.4 Comparison of function $C_\mu(S, \Omega)$ on S-Ω plane
(left: Kimura & Hosoda (2003)(6), right: Ali, Hosoda and Kimura (2007)(7))

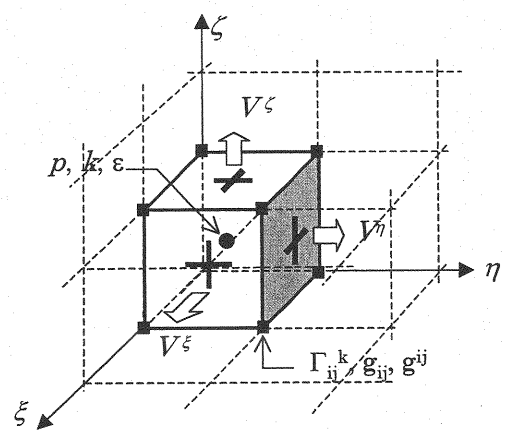

Fig. 5 Arrangement of hydraulic variables and metric tensors on full staggered grid

and Hosoda (6) has a sharp edge, which means that the value of the function changes suddenly around the region of $S = \Omega$. This feature seems to be physically unsound. A typical flow which satisfies $S = \Omega$ is a simple shear flow. The models with functions of Φ are therefore not suitable for flows with vortex formations from a simple shear layer due to K-H instability. We adopted the model by Ali et al. (7) as the non-linear k-ε model for the present second-order non-linear model.

(3) The third order non-linear k-ε model

The constitutive equation of the third order non-linear k-ε model can be obtained by adding the following the third order terms to the second order constitutive equation (Eq. 9).

$$[\text{Third order terms}] = -\frac{k^2}{\varepsilon^2}\nu_t\left(C_4 T_A^{\ ij} + C_5 T_B^{\ ij}\right) \tag{21}$$

where

$$T_A^{\ ij} = \Omega^{i\alpha} g_{\alpha k} S^{k\beta} g_{\beta l} S^{lj} - S^{i\alpha} g_{\alpha k} S^{k\beta} g_{\beta l} \Omega^{lj} \tag{22}$$

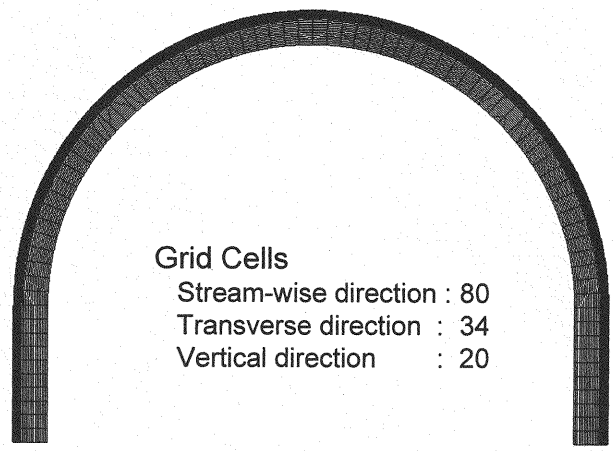

Fig.6 Computational grid in a horizontal plane used in Case A

$$T_B^{ij} = \Omega^{i\alpha} g_{\alpha k} \Omega^{k\beta} g_{\beta l} S^{lj} + S^{i\alpha} g_{\alpha k} \Omega^{k\beta} g_{\beta l} \Omega^{lj} - \frac{2}{3} S^{m\alpha} g_{\alpha n} \Omega^{n\beta} g_{\beta o} \Omega^{o\gamma} g_{\gamma m} g^{ij} \tag{22}$$

Two model coefficients, C_4 and C_5, in the third order terms in Eq. 21 are tuned by trial and error after several cases of preliminary computations as

$$C_4 = 0, \; C_5 = 0.01 f_M \tag{23}$$

Outline of the Computational Method

(1) Computational scheme

The differential equations governing the mean-velocities and the turbulence field are solved with the finite volume method on a full-staggered grid system. The arrangement of hydraulic variables on a full-staggered grid is shown in Fig. 5. The metric tensor and Christoffel's symbol are defined only at grid points to save computer memory and the values at other positions are interpolated at each computational step.

The QUICK scheme with the second order accuracy in space is applied to the convective inertia terms and the central differencing is used for the diffusion terms in the momentum equations. The hybrid central upwind scheme is applied to the k and ε equations for the computational stability. The Adams-Bashforth scheme with second-order accuracy in time is used for time integration in each equation. The basic equations are discretized as fully explicit forms and are solved successively along the time step. The pressure field is solved by using an iterative procedure at each time step by using the SOLA algorithm proposed by Hirt et al. (9).

(2) Computational domains and computational grids

We adopted the experimental result by Booij (1) to evaluate the computational models. Two different computational domains (Case A and Case B) are tested.

In Case A, the whole U-type domain of the channel is included in the computation. Fig. 6 shows the computational grid used in Case A. Numbers of grid points are 80 in the longitudinal direction, 34 in transverse direction and 20 in the depth-wise direction. In order to obtain the inlet boundary conditions, a preliminary computation in a straight channel (length = 1.0m) was performed by using cyclic boundary conditions at inlet and outlet boundaries. The well developed velocity distribution and turbulence quantities in the preliminary computation

Table 3 Numbers of grid cells in 4 cases for grid sensitivity analysis

	x	y	z
Grid I	20	68	40
Grid II	10	34	20
Grid III	5	17	10
Grid IV	5	13	10

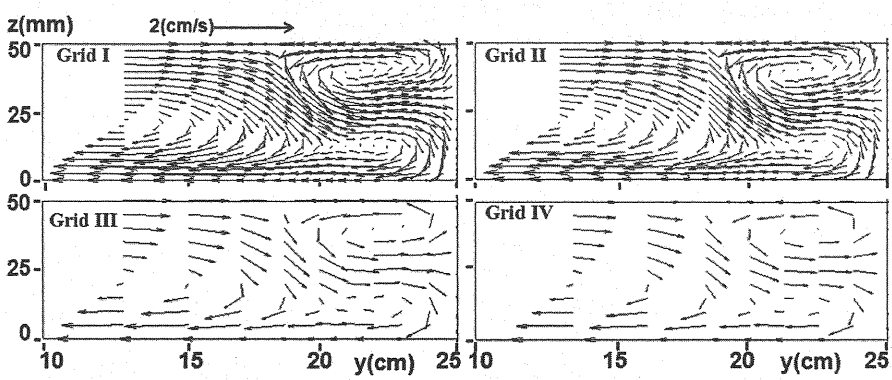

Fig.7 Comparison of cross-sectional flow patterns with 4 type s of computational grids in Case B

are used at the inlet boundary in the computations in whole U-type channel. At the downstream end of the U-type computational domain, the longitudinal gradients of all variables are assumed to be zero (0-gradient outlet conditions).

In Case B, only an arc with the center angle = 30° is included in the computational domain and cyclic boundary conditions are used at inlet and outlet boundaries in all velocity components and turbulence quantities. This computation corresponds to the well-developed curved channel flow in an infinitely long circular channel. The channel slope was adjusted during the computations at every 10 second, yielding the same discharge as in the experiment (Q = 5ℓ/s).

(3) Boundary conditions

Since the present turbulence model is a high Reynolds number type, the wall function approach is applied as the wall boundary conditions for k and ε. The wall friction is evaluated by means of the log-law.

The free surface elevation can be easily calculated by the following simple equation (Eq. 24) since the contravariant components of the velocity vector are used in the basic equations (Takizawa et al. (10)).

$$\Delta h = \sqrt{g_{33}} V^3 \Delta t \tag{24}$$

where Δt = time increment and Δh = surface elevation during Δt. The computational grid is moved in the vertical direction according with the water surface elevation. The ratio of grid intervals in the vertical direction is kept constant during the grid motion. Kimura et al. (11) showed that this computational method for free surface motion can capture well the backwater elevation around a bridge pier.

To consider the rapid attenuation of turbulent intensities in the vertical direction near the free surface, the eddy viscosity is multiplied by means of the following damping function (Hosoda (12))

$$f_s = 1 - \exp\left(-B_f \frac{(h-y)\varepsilon_s}{k_s^{3/2}} \right) \quad , \quad (B_f = 10) \tag{25}$$

where sub-s indicates the value at the surface layer. Since this function takes the value between 0 and 1, the function

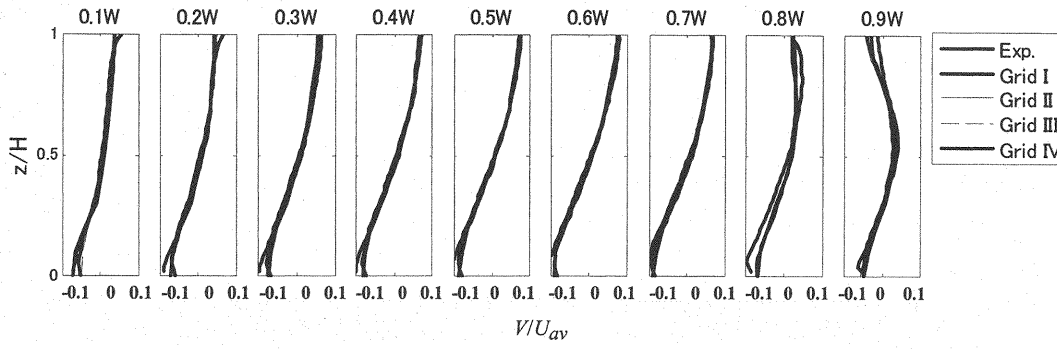

Fig.8 Comparison velocity profiles V with different computational grids

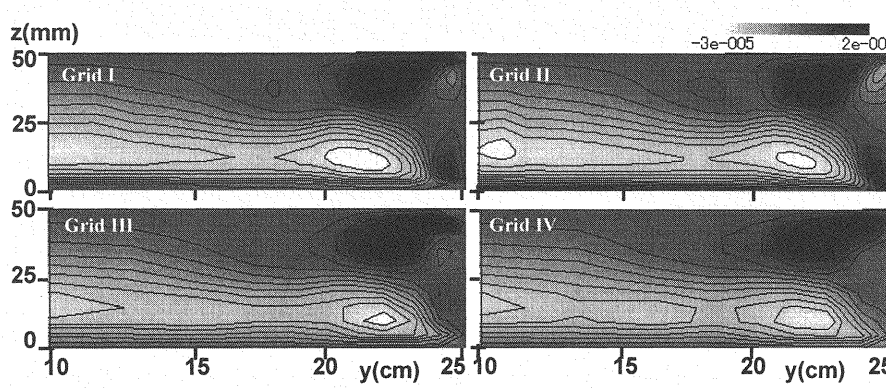

Fig.9 Comparison of Reynolds stress $\overline{vw}$ with different grid

does not change the realizability conditions. In addition, the value of this function is very close to 1 except the surface layer under the present hydraulic conditions. Therefore, this function only affects the surface boundary conditions of turbulence. The turbulence dissipation rate at the surface layer is evaluated by using the following formula proposed by Sugiyama et al. (13) to calculate the secondary currents of the second kind.

$$\varepsilon_s = \frac{C_{\mu 0}^{3/4} k_s^{3/2}}{0.4\Delta s}, \quad (C_{\mu 0} = 0.09) \tag{26}$$

where Δs is the distance from the surface to the first definition point of ε.

(4) Initial conditions

At the beginning of the calculation, U (= velocity in the longitudinal direction (x-direction)) = U_a (=averaged bulk velocity), V (= velocity in the transverse direction (y-direction)) = 0, $k = k_{in}$ and $\varepsilon = \varepsilon_{in}$ (k_{in} and ε_{in} are the values of k and ε at the inlet boundary) are specified over the whole computational domain. In order to avoid the influence of the initial conditions, the numerical results after 200 seconds from the initial conditions are used for analysis.

RESULTS AND DISCUSSIONS

Grid Sensitivity Analysis

Grid sensitivity was examined by using 4 different types of computational grids to consider the appropriate grid resolution. The computational domain of Case B was used for this analysis to reduce CPU time. The numbers of

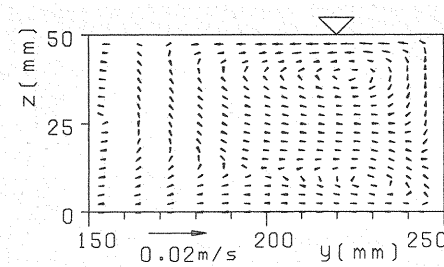

Fig.10 Cross-sectional flow pattern obtained in the preliminary computation in a straight channel (The second order non-linear model)

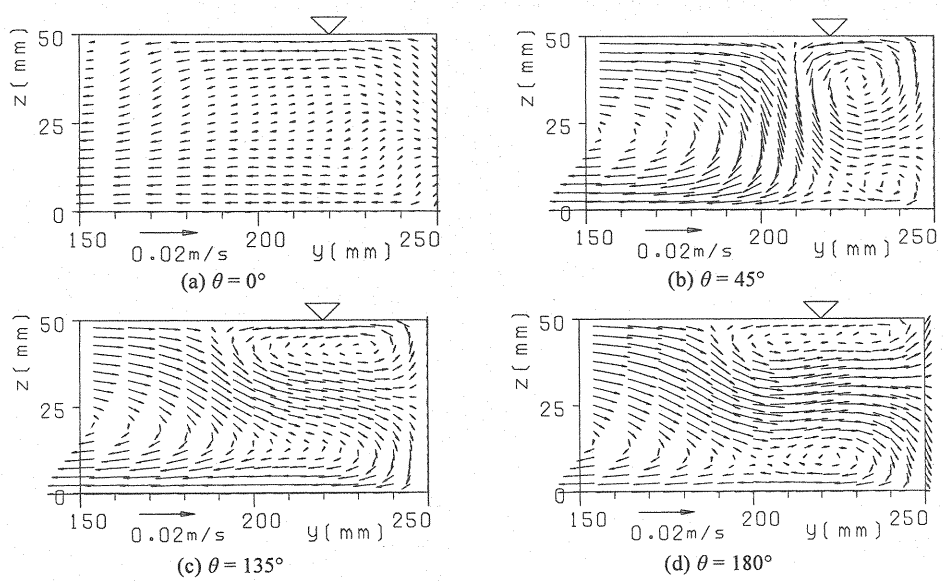

Fig.11 Cross-sectional flow patterns at 4 different cross-sections in Case A (The second-order non-linear model)

the 4 types of grids are listed in Table 3. Fig. 7 shows a comparison of cross-sectional flow patterns computed with 4 types of grids. In all cases, even in the very coarse grid of Grid IV, an outer-bank cell is clearly generated. The flow feature in each case is very similar and is in good agreement with the experimental result shown in Fig 2.

Fig. 8 shows the comparison of velocity profiles at $y = 0.9B$. The profiles by 4 types of computational grids are almost identical. However, careful observation reveals that the computational results with finer grids agree with the experimental results better than the results with coarser grids. Fig. 9 shows the profiles of Reynolds stress $\overline{vw}$ at a cross-section. Blanckaert et al. (14) showed that this component of Reynolds stresses plays a significant role in generating the outer-bank cell. The computational result with each grid shows that the large value of $\overline{vw}$ is generated near the corner between the surface and the outer-bank. Comparisons of the results in the different grids indicate that Grid II has enough resolution to consider the cross-sectional flow pattern and turbulence structures. Hereafter, Grid II is used for all computations in Case B.

Comparison of results with different computational domains

(1) Flow pattern in the preliminary computation in a straight channel

A preliminary computation in a straight open channel flow was performed to obtain inlet boundary conditions

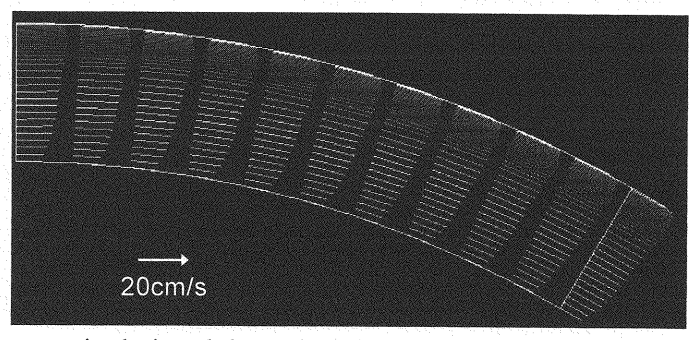

Fig.12 Flow pattern in a horizontal plane at the surface in Case B (The second order non-linear model)

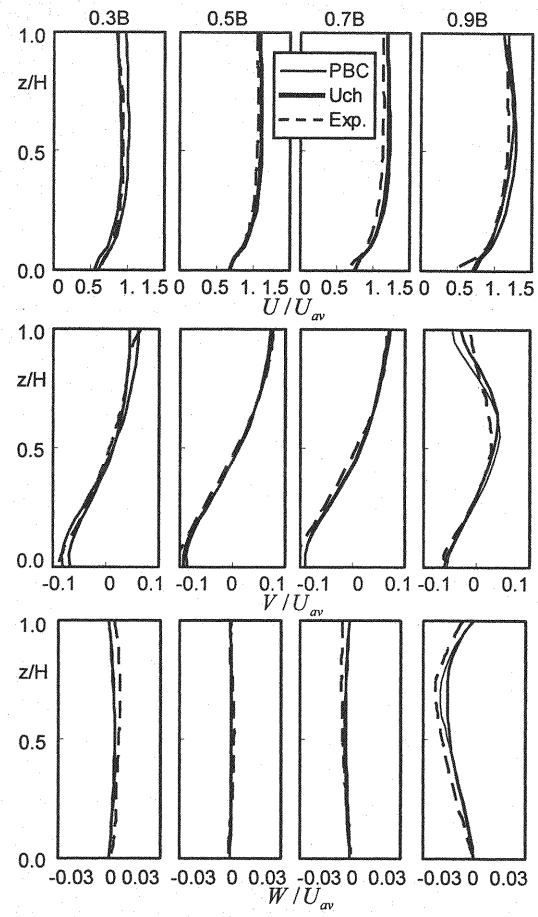

Fig.13 Velocity profiles at 4 sections (The second order model, Uch: Case A, PBC: Case B, Exp: experiment)

for Case A. Fig. 10 shows the flow pattern in a cross-section obtained in the preliminary computation. We can observe two vortices near the outer-bank. These vortices are secondary currents of second kind caused by the anisotropy of turbulence. The location of the vortex near the surface coincides with the location of the outer-bank cell observed in the laboratory test (see Fig. 2) though the maximum cross-sectional velocity in the computation is less than 30% of the velocity in the outer-bank cell.

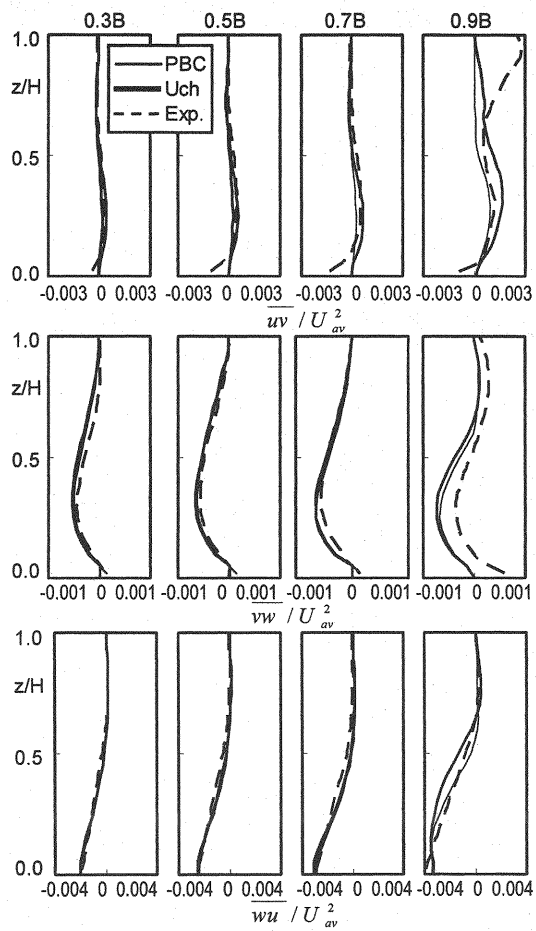

Fig.14 Reynolds stress profiles at 4 sections (The second order model, Uch: Case A, PBC: Case B, Exp: experiment)

(2) Flow patterns in the computation in a U-type channel bend

The computation in the U-type channel bend of Case A was performed by using all velocity components, k and ε obtained by the preliminary computation as the inlet boundary conditions. The computational grid shown in Fig. 6 was used for this computation. The cross-section of the grid is same as that of Grid II in Case B. Though the flow became almost steady at t=200 (sec), we used the flows at t=400 (sec) for following analysis in order to avoid the influence of initial conditions.

Fig. 11 shows the cross-sectional flow patterns in the computation at θ= 0°, 45°, 135° and 180°. The second order non-linear k-ε model was used for this computation. The vortices due to anisotropy of turbulence in the preliminary computations are completely disappeared at θ= 0°. The reason for this seems to be that the sudden change of the curvature radius (∞→4.1m) causes a strong inward pressure from the outer-bank and rapidly deforms the vortices. A vortex in a circular shape can be observed again near the outer-bank at θ= 45°. The shape of the outer-bank cell is gradually stretched in a horizontal direction as the vortex moves in a downstream direction. The flow pattern at θ= 135° in the computation is in reasonable agreement with the experimental results (see Fig. 2) though the computed horizontal length of the outer-bank cell is somewhat larger than the experimental results.

Generally, the water surface slope in the lateral direction plays an important role in determining the flow structure particularly in cases where there are sharp bends. However, in the present condition of a mild bend, the

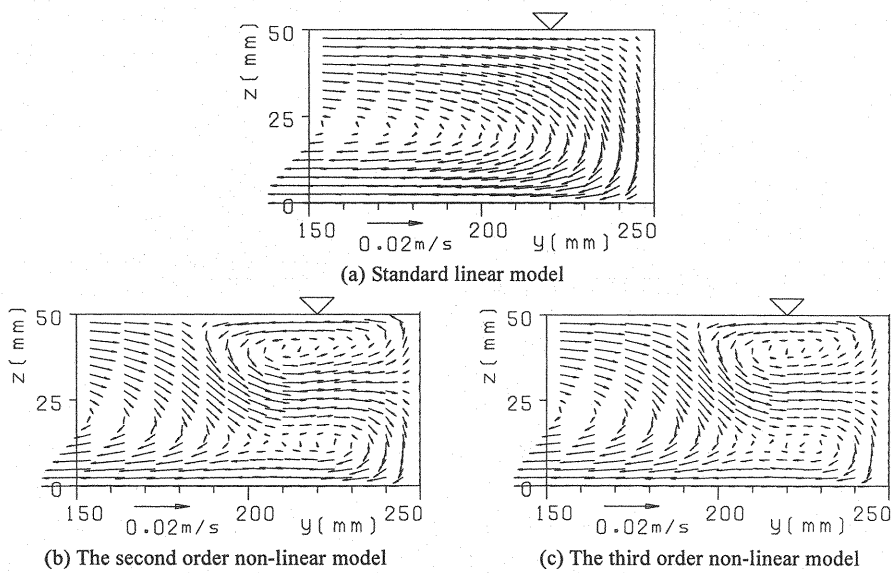

(a) Standard linear model

(b) The second order non-linear model

(c) The third order non-linear model

Fig.15 Comparison of the cross-sectional flow patterns by different turbulence models

surface slope is very small. In the present computational results, the difference of the water levels at the outer and inner bank is only 0.4 ~ 0.5mm. That means the lateral surface slope is less than 1/1000.

Result in Case B

(1) Horizontal flow pattern

Fig. 12 shows the horizontal flow pattern in the horizontal plane at the surface obtained in the computation of Case B using the second order non-linear k-ε model. The computed flow became almost steady at t = 50 (sec) and the flow in Fig. 12 is the result at t = 100 (sec). This figure shows that the velocity near the outer-bank becomes larger than the velocity near the inner-bank, which is a well-known typical flow feature in a mildly curved channel flow.

(2) Comparison with the result in Case A

Fig. 13 shows the time mean velocity profiles along 4 vertical sections at y' = 0.3B, 0.5B, 0.7B and 0.9B (y': distance from the inner-bank, B: channel width (= 50cm)). The velocity profiles obtained in Case A and in the laboratory test at θ = 135° are shown together. All velocity components at 4 sections in Case B agree well with the experimental results. The results in Case B are also in line with the results in Case A. In the velocity profile U at 0.9B, the inverse velocity gradient can be seen in both experimental and numerical results although the inverse slope in the numerical results is slightly larger than the experimental results. This finding means that the unbalance of the centrifugal force, which drives the outer-bank cell, is a little bit larger in the numerical results than in the experimental result. Fig. 14 shows a comparison of Reynolds stresses in two computational results and the experimental result along the same 4 lines. The two computational results are again very similar. The agreement of the computational results with the experimental results is satisfactory except for the $\overline{uv}$ component near the surface at y' = 0.9B. The $\overline{uv}$ in the experiment becomes larger near the surface at y' = 0.9B though the computational result is almost zero at the surface. The reason is still not known.

The computational data in Case A at θ = 135° agree well with the results in Case B in both Fig. 13 and Fig. 14. This agreement reveals that the flow at θ = 135° in the U-type channel is a well-developed curved channel flow

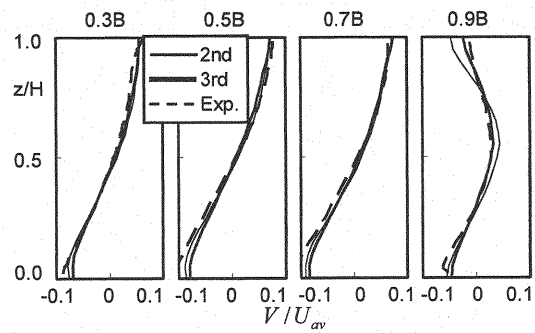

Fig.16 Comparison of mean velocity V
(2nd: The second order non-linear model, 3rd: The third order non-linear model)

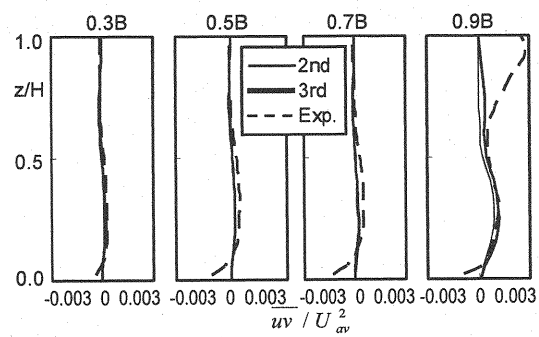

Fig.17 Comparison of $\overline{uv}$ (2nd: The second order non-linear model, 3rd: The third order non-linear model)

because the flow in Case B is equivalent to the flow in an infinite circular channel. This finding also implies that it is sufficient to use the computational domain of Case B to examine time mean cross-sectional flows. Therefore, any discussions hereafter will consider the results of only Case B for the sake of computational efficiency.

(3) Effect of the order of the constitutive equations

Fig. 15 shows a comparison of cross-sectional flow patterns computed using the standard linear model, the second order non-linear model and the third order non-linear model. The standard linear model could not capture the outer-bank cell at all and other two non-liner models could generate it. The horizontal scale of the outer-bank cell is slightly larger than the experimental results by the second order model while the shape of the outer-bank cell by the third order model agrees closely with the experimental results. The shape of the outer-bank cell by the second order model is very similar to the results in Case A at $\theta = 135°$ with the second order model (see Fig. 11 (c)).

Fig. 16 shows the comparison of profiles of the mean velocity in the transverse direction (=V) computed by the second order and third order models. The profile at $y' = 0.9B$ by the third order model shows better agreement with the experimental result. Fig. 17 shows a comparison of Reynolds stress $\overline{uv}$ computed by the two models. The large value of observed at $y' = 0.9B$ near the surface is still not reproduced by the third order model. It should be noted that the large value of $\overline{uv}$ near the surface along the outer-bank has been captured by using LES by van Balen et al. (15). Therefore, further model refinement is necessary to improve the present non-linear RANS models.

(4) Effect of eddy viscosity coefficient

Christensen et al. (3) has reported that the outer-bank cell can be captured by the standard linear k-ε model if the curvature radius is small ($R/H < 16$). This result indicates that anisotropy of turbulence is not only the cause of the outer-bank cell. In order to consider this matter, we performed the computation by using the standard linear model in cases of smaller curvature radii. Fig. 18 shows the computational results with the standard linear model in $R = 1.15$

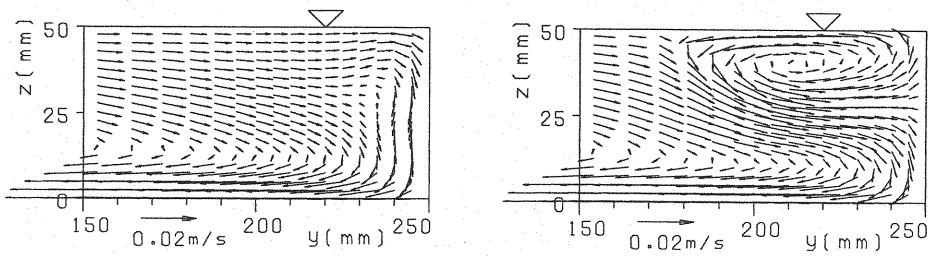

a) R = 1.15m (b) R = 1.1m

Fig.18 Comparison of the cross-sectional flow patterns under smaller curvature radii by the standard linear k-ε model

m and 1.1 m. Since the outer-bank cell is generated only for the case of $R \leq 1.1$ m, the threshold of R/H (H = 5cm) in this case is around 22.

De Vriend (5) reported that the eddy viscosity plays an important role to induce the outer-bank cell. In order to check the effect of eddy viscosity, a computation is performed using a modified linear model. The modified linear model is constructed with linear constitutive equation (Eq. 8) and the functional form of C_μ (Eqs. 17 and 18) used in the non-linear models. The eddy viscosity of this model decreases as the parameter S or Ω becomes larger. It has been pointed out that the standard k-ε model generates excessive turbulence kinetic energy which makes the computational results too smooth. The modified model can be recognized as a model which corrects the drawback of the standard k-ε model.

In the computational result by the modified model, the outer-bank cell can be generated in case of larger curvature radius compared with the standard model. The threshold of the outer-bank cell with the modified model became R/H = 24. This finding indicates that the model with smaller eddy viscosity generates the outer-bank cell more easily in a milder curved channel flow. De Vriend (5) proposed a modified Dean number, which can be obtained by replacing the dynamic viscosity in the Dean number by an eddy viscosity ($De' = De\cdot(\nu/\nu_t)$), as a governing parameter of the outer-bank cell. The present computational results show that the parameters expressing the criterion for generating an outer-bank cell should include an eddy viscosity coefficient. From this viewpoint, the modified Dean number seems to be a reasonable approach even though the validity of the modified Dean number as the criterion should be examined further.

It is clear that the outer-bank cell in a turbulent flow is caused by a rather complicated mechanism with interaction between turbulence anisotropy and the unbalance of the centrifugal force and the local pressure gradient. Therefore, there might be several governing parameters including De (Dean number) and De' (modified Dean number). Further considerations are necessary to determine the governing parameters and their thresholds. The RANS computational model proposed in this study, which has striking priority in computational efficiency, will become a useful tool in further studies.

CONCLUDING REMARKS

The linear and non-linear k-ε models were applied to the mildly curved open channel flow and the results were discussed focusing on characteristics of the outer-bank cell. The main findings are summarized as follows.

1) Through the grid sensitivity analysis, it is observed that the non-linear RANS model can generate the outer-bank cell with a rather coarse grid (e.g., number of grid cells in a cross-section: 10 (vertical direction) × 13 (transverse direction)).
2) The computational flow pattern at θ=135° in the U-shape channel agrees well with the computational results of a circular channel element with cyclic boundary conditions. Therefore, it is presumed that the flow at θ = 135° is

equivalent to a well-developed curved channel flow in an infinite circular channel.

3) The outer-bank cell was generated only by the non-linear models. The shape of the outer-bank cell was reproduced by the third order model better than the second order model.
4) The second and third order non-liner models could reproduce mean velocity and Reynolds stress profiles satisfactory. However, the two models could not capture the large value of $\overline{uv}$ near the surface at the outer-bank, which was observed in the laboratory tests and the previous LES computation.
5) The maximum value of R/H, which yields the outer-bank cell for the linear model, was 22. When we use a modified linear model with smaller eddy viscosity, the threshold of R/H becomes larger.

It was pointed out that the combination of the present non-linear RANS model and the smaller computational domain with cyclic boundary conditions could capture the outer-bank cell efficiently. The method may be a useful tool for carrying out further investigations on governing parameters and their detailed conditions for generating the outer-bank cell.

ACKNOWLEDGEMENTS

The authors are grateful to R. Booij at Delft University of Technology and K. Blanckaert at EPFL for kind advices and fruitful discussions.

REFERENCES

1. Booij, R.: Measurements and large eddy simulations of the flows in some curved flumes, Journal of Turbulence, Vol. 4, pp.1-17, 2003.
2. Blanckaert, K.: Flow and turbulence in sharp open-channel bends, PhD thesis 2545, Ecole Polytechnique Federale Lausanne, Switzerland, 2002.
3. Christensen, B., Gislason, K. and Fredsoe, J.: Secondary turbulent flow in an infinite bend, 1st RCEM Symp., Genova, Italy, vol.1, pp.543-553, 1999.
4. Jia, Y,. Blanckaert, K. & S. Y. Wang, S.: Simulation of secondary flow in curved channels, Advances in Fluid Modeling & Turbulence Measurements, World Scientific, pp.55-62, 2001.
5. De Vriend, H. J.: Steady flow in shallow channel bends, Rep.81-3, Lab. Fluid Mech., Dept. Civil Eng., Delft University of Technology, 1981.
6. Kimura, I. and Hosoda, T.: A non-linear k-ε model with realizability for prediction of flows around bluff bodies. International Journal for Numerical Methods in Fluids, Vol.42, pp.813-837, 2003.
7. Ali, M. S., Hosoda, T. and Kimura, I.: A non-linear k-ε model to predict the spatial change of turbulent structures in large scale vortices, J. Applied Mech., JSCE, Vol.10, pp.723-732, 2007.
8. Craft, T. J., Launder, B. E. and Suga, K.: Extending the applicability of eddy viscosity models through the use of deformation invariants and non-linear elements, Proc. 5th IAHR conference on Refined Modeling and Measurement, Paris, pp.125-132, 1993.
9. Hirt, C. W., Nichols, B. D. & Romero, N. C.: SOLA - a numerical solution algorithm for transient fluid flows. Los Alamos Scientific Report, LA-5852, 1975.
10. Takizawa, A., Koshizuka, S. & Kondo, S.: Generalization of physical component boundary fitted co-ordinate (PCBFC) method for the analysis of free-surface flow, International Journal for Numerical Methods in Fluids, Vol.15, pp.1213-1237, 1992.
11. Kimura, I., Hosoda, T. & Onda, S.: Predictions of turbulent flows around a bridge pier using various numerical models, River Flow 2006, Lisbon, Portugal, Balkema, Vol.1, pp.767-775, 2006.

12. Hosoda, T.: Turbulent diffusion mechanism in open channel flows, Ph.D. Thesis, Kyoto University, 1990 (in Japanese).
13. Sugiyama, H., Akiyama, M. & Matsubara, T.: Numerical simulation of compound open channel flow on turbulence with a Reynolds stress model, Journal of Hydraulic, Coastal and Environmental Engineering, 515 / II-31: 55-65, 1995 (in Japanese).
14. Blanckaert, K. & de Vriend, H. J.: Secondary flow in sharp open-channel bends, J. Fluid Mech., Vol.498, pp.353-380, 2004.
15. Van Balen, W., Booij, R. & Uijttewaal, W.S.J.: Large eddy simulation of the flow through a curved flume, Proc. 5th Int. Symp. Envir. Hydr., Arizona, USA, (CD-ROM), 2007.

APPENDIX – NOTATION

The following symbols are used in this paper:

g = determinant of g_{ij};

g_{ij} = covariant component of metric tensor;

g^{ij} = contravariant component of metric tensor;

k = turbulent kinetic energy;

p = pressure;

t = time;

F^i = contravariant component of gravitational acceleration;

B = channel width;

B_f = model constant (=10);

C_1-C_5 = model coefficients;

$C_{\varepsilon 1}$ = model constant (= 1.44);

$C_{\varepsilon 2}$ = model constant (= 1.92);

C_μ = model coefficient for eddy viscosity;

De = Dean number;

De' = modified Dean number;

Q = flow discharge;

R = curvature radius of curved channel;

Re = Reynolds number;

S = strain parameter;

V^i = contravariant component of the velocity vector of flow;

W^i = contravariant component of the velocity vector of grid motion;

ε = turbulent energy dissipation rate;

μ = discharge coefficient of the step flow formula;

ν = molecular kinematic viscosity coefficient;

ν_t = eddy viscosity coefficient;

θ = center angle of the considered cross section;

ρ = density of water;

ξ^I = generalized curvilinear coordinate;

σ_k = model constant (=1.0);

σ_ε = model constant (=1.3);

Δs = the distance between the surface and the first definition point of ε;

Δt = time increment;

Γ_{ij}^k = Christoffel's symbol;

Ω = rotation parameter; and

Φ = maximum of rotation and strain parameters (=max[S,Ω]).

(Received Sep 26, 2008 ; revised Sep 08, 2009)